

High-Quality Spatial Reconstruction and Orthoimage Generation Using Efficient 2D Gaussian Splatting

Qian Wang^{1,*}, Zhihao Zhan^{2,*}, Jialei He¹, Zhituo Tu¹, Xiang Zhu^{2,†} and Jie Yuan^{1,†}

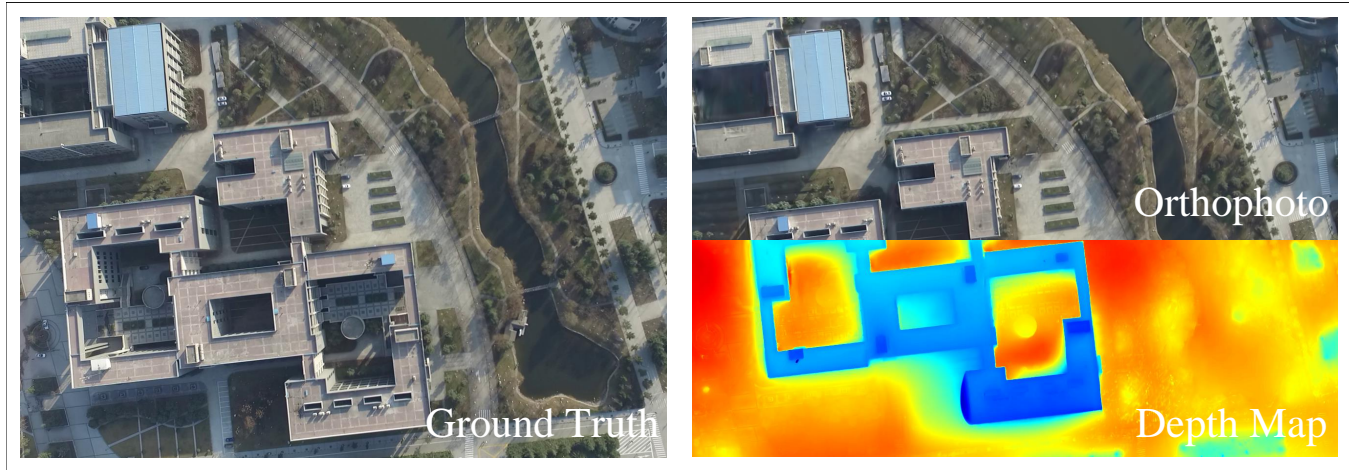


Fig. 1: Presentation of the orthophoto and depth map we generated. Our method effectively corrects image distortion caused by perspective, preserves scene details, and generates accurate terrain information.

Abstract—Highly accurate geometric precision and dense image features characterize True Digital Orthophoto Maps (TDOMs), which are in great demand for applications such as urban planning, infrastructure management, and environmental monitoring. Traditional TDOM generation methods need sophisticated processes, such as Digital Surface Models (DSM) and occlusion detection, which are computationally expensive and prone to errors. This work presents an alternative technique rooted in 2D Gaussian Splatting (2DGS), free of explicit DSM and occlusion detection. With depth map generation, spatial information for every pixel within the TDOM is retrieved and can reconstruct the scene with high precision. Divide-and-conquer strategy achieves excellent GS training and rendering with high-resolution TDOMs at a lower resource cost, which preserves higher quality of rendering on complex terrain and thin structure without a decrease in efficiency. Experimental results demonstrate the efficiency of large-scale scene reconstruction and high-precision terrain modeling. This approach provides accurate spatial data, which assists users in better planning and decision-making based on maps.

I. INTRODUCTION

Digital Orthophoto Maps (DOMs) from Unmanned Aerial Vehicle (UAV) surveying provide dense textural and geometric data, useful in fields like agriculture [1], environmental monitoring [2], and disaster assessment [3]. DOMs are typically created by combining a Digital Elevation Model (DEM)

with images captured from a fixed perspective, resulting in a nadir image of the target surface to correct projection distortion due to terrain and oblique photography [4]. Yet, facade occlusions of object can produce artifacts and incorrect geometry. True Digital Orthophoto Maps (TDOMs) address this by incorporating Digital Surface Models (DSM) and using visibility checks to reduce occlusion effects and enhance map accuracy [5].

Over the past decades, numerous methods have been suggested for the generation of True Digital Orthophoto Maps (TDOMs). The Z-buffer method [6], [7], [8], for example, resolves visibility by keeping a note of distances between object points and perspective center corresponding to image pixels and selecting the nearest point. Another method identifies occlusions from the angle between the perspective center and Digital Surface Model (DSM) units with adaptive radial and spiral sweeps, and according to the height analysis of the light rays [9]. In recent years, few learning-based methods have been used to generate TDOMs, but have the drawbacks of limited generalization and high dependence on LiDAR data. For instance, Ebrahimikia and Hosseinaveh’s method [10] identifies building edges in images and alters the DSM, whereas other methods directly produce TDOMs through the use of Generative Adversarial Networks (GANs) [11], [12].

Neural Radiance Fields (NeRF) [13], [14] and 3D Gaussian Splatting (3DGS) [15], new rendering-based methods, have introduced new solutions to the development of True Digital Orthophoto Maps (TDOMs). NeRF is made more efficient

* Qian Wang and Zhihao Zhan contributed equally to this work.

† Xiang Zhu (xzhu@topxgun.com) and Jie Yuan (yuanjie@nju.edu.cn) are the corresponding authors.

¹ School of Electronic Science and Engineering, Nanjing University, Nanjing, 210046, China.

² TopXGun Robotics, Nanjing, 211100, China.

with implicit 3D scene representation and differentiable rendering, further aided by approaches such as Plenoxels [16] and Ortho-NeRF [17]. However, NeRF is still troubled by long training times and heavy rendering loads that hinder its real-time implementation. Conversely, 3DGS uses Gaussian kernels to encode 3D scene data explicitly and accelerates training and rendering through parallel processing, e.g., TOrtho-Gaussian [18], at more than 100 frames per second. The scalability limitations of 3DGS in large-scale scene primarily stem from the hardware-dependent constraint that the number of 3D Gaussian kernels is bounded by the video memory capacity of graphics processing units. Furthermore, fidelity needs to be prioritized, particularly when dealing with reflections and slender structures, where blurring and aliasing may occur.

This work describes a new TDOM-generation method based on a variant of 3DGS called 2DGS [19]. Surface reconstruction quality and perspective consistency are essential for TDOM generation. 2DGS resolves the perspective inconsistency of 3DGS by enhancing both geometric representation and rendering mechanisms. By utilizing normal information to refine surface structures, 2DGS yields higher-quality 3D reconstructions. Many TDOM applications require depth information to accurately represent the 3D structure of the scene, and our method addresses this by extracting the corresponding depth maps during the rendering process, thereby enhancing the overall reconstruction accuracy. Inspired by VastGaussian [20] and CityGaussian [21], we adopt a divide-and-conquer strategy to enable large-scale 2DGS training and high-resolution TDOM rendering with limited computational resources, as demonstrated in Fig 1.

In summary, we make the following contributions:

- 1) We propose a TDOM-generation framework based on a highly efficient differentiable 2D Gaussian renderer, which ensures geometric fidelity and consistency across multi-view observations.
- 2) We introduce a geometry-aware depth estimation module that directly derives depth maps during the rendering process.
- 3) Our approach leverages a divide-and-conquer strategy to enable efficient large-scene reconstruction and high-resolution TDOM rendering under constrained computational resources, bridging the gap between quality and practicality.

II. RELATED WORKS

A. Traditional TDOM Generation Methods

Traditional TDOM generation methods require DSM priors. The key steps in traditional TDOM generation involve analyzing the visibility of surface objects through occlusion detection and compensating for occluded areas using information from adjacent images.

The Z-buffer method [6] is one of the earliest proposed visibility analysis algorithms, characterized by its simplicity in principle, but exhibits strong dependence on a high-precision DSM. Subsequently, the angle-based occlusion

detection algorithm [9] was proposed, which identified occlusion by sequentially analyzing the angles of projected rays along radial directions in the DSM. Inspired by ray tracing algorithms, Wang et al. [22] optimized the algorithm to ensure smooth and stable edge detection while reducing computation time. Alternative approaches include the height-based shadow detection methodology initially developed by Bang [23]. This method identifies occlusion by comparing the height of projected rays with the DSM height at regular horizontal intervals. There is also a vector polygon-based algorithm [24], [25], which projects the vectors polygons representing building surfaces into the image space and evaluates occupancy priority in overlapping areas to acquire the actual coverage relationship. Wang et al. [26] introduced a method for enhancing shadow information in color aerial imagery and proposed an information lost area compensation approach based on texture matching.

Each of these methods has distinct characteristics and specific application scenarios. However, they also come with inherent limitations. For instance, they rely heavily on high-quality DSM or DBM, the acquisition of which is often costly. Moreover, these methods still face challenges in achieving precise edge detection [27], natural texture compensation [12], and a streamlined, efficient workflow [28], [29]. These difficulties become even more pronounced when generating large-scale TDOM [30].

B. Deep Learning-based Methods

Recent methodological advancements have increasingly adopted deep learning frameworks to replace some intermediate steps in traditional TDOM generation workflows [12], [31], [32]. For example, Urban-SnowflakeNet [32] utilizes a deep learning network to extract features from preprocessed rooftop point clouds. It reconstructs building point clouds to aid in DSM rectification and TDOM generation, thereby effectively reducing distortions at building edges in urban scenes. However, these methods still rely on a combination of vision and LiDAR, requiring high-quality LiDAR point clouds and potentially failing in certain scenarios.

C. Differentiable Rendering-based Methods

The new view synthesis method based on differentiable volume rendering has significantly improved the quality of reconstructed images, providing a novel approach for pure vision-based TDOM generation. By integrating differentiable volume rendering, NeRF[33] trains an implicit neural radiance field, achieving remarkable-fidelity and highly continuous scene reconstruction. Many speed-optimized variants of NeRF, such as Instant-NGP [34] and Plenoxels [16], have been applied to TDOM rendering, achieving image quality on par with traditional approaches [35], [17].

NeRF-based methods suffer from a major drawback in rendering efficiency. In contrast, 3DGS [36], proposed by Bernhard et al., explicitly represents scenes with 3D Gaussian spheres and performs splatting rendering via a high-speed differentiable rasterizer, enabling real-time, high-quality rendering. TOrtho-Gaussian [18], a recent approach, addresses

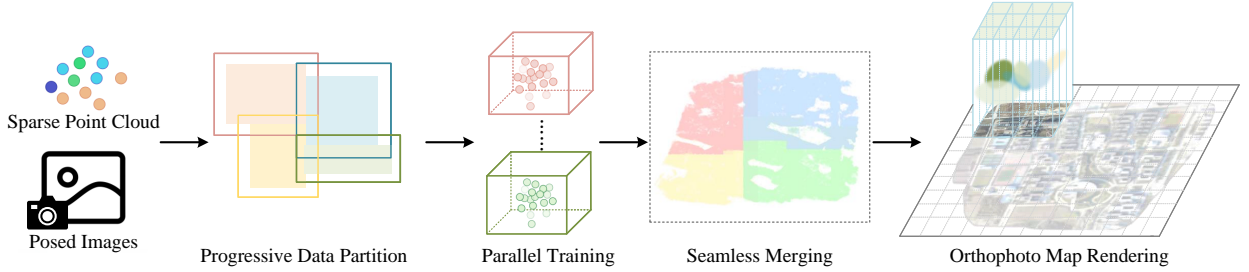


Fig. 2: Illustration of our pipeline. The input consists of sparse point clouds and images with poses. After progressive data partitioning, training is conducted in parallel on different GPUs. Eventually, the trained Gaussians are projected onto an image plane using an orthographic projection method, with the complete TDOM rendered through batch rasterization. Simultaneously, the corresponding depth images are generated.

GPU memory limitations caused by the growing number of Gaussian spheres in large-scale scenes by employing a divide-and-conquer strategy. It circumvents the complexity of traditional visibility analysis and shadow compensation algorithms while ensuring computational efficiency, demonstrating great potential for 3DGS-based TDOM generation methods.

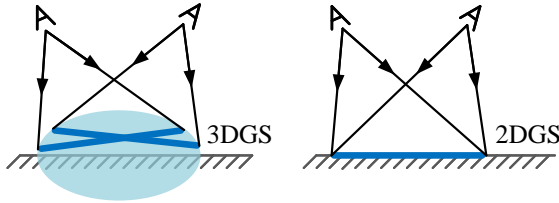


Fig. 3: Explanation of the differences between 3DGS and 2DGS. For 3DGS, the surfaces observed from different views are distinct and almost do not represent the actual surfaces, while the same plane is observed from any view with 2DGS.

III. METHOD

The entire TDOM production process is shown in Fig 2. First, we initiate the point cloud as 2D Gaussians with original 2DGS training strategy presented in Section III-A. The orthographic camera model and the depth map generation method are described respectively in Section III-B and Section III-C. For the sake of training large-scale scenes, we employ a divide-and-conquer approach, and the seamlessly merged 2D Gaussians are rendered using Batch Rasterization to obtain high-resolution TDOM, which is detailed in Section III-D.

A. Preliminaries

3DGS represents the entire scene with a set of 3D Gaussian ellipsoids $G(\mathbf{x})$, which are initialized from point clouds of Structure-from-Motion (SfM)[37]. 3D Gaussian primitives can be represented by the Gaussian center μ and the covariance matrix Σ :

$$G(\mathbf{x}) = \exp\left(-\frac{1}{2}(\mathbf{x} - \mu)^T \Sigma (\mathbf{x} - \mu)\right) \quad (1)$$

where the covariance matrix $\Sigma = \mathbf{R}\mathbf{S}\mathbf{S}^T\mathbf{R}^T$ is decomposed into a scaling matrix \mathbf{S} and a rotation matrix \mathbf{S} . Moreover, the properties of Gaussian primitives also include the opacity α and the spherical harmonic (SH) coefficients. To render an image, 3D Gaussian primitives must be projected onto the 2D image plane. Under a given viewpoint V_k , the projected 2D covariance matrix Σ_k in projection space can be represented with the view transformation matrix \mathbf{W} and the projective transformation matrix \mathbf{J} :

$$\Sigma_k = \mathbf{J}\mathbf{W}\Sigma\mathbf{W}^T\mathbf{J}^T \quad (2)$$

By replacing the Gaussian center μ and the covariance matrix Σ with the transformed μ_k and Σ_k , the Gaussian primitive G^{2D} on the image plane is obtained. After sorting N Gaussian primitives based on depth, 3DGS renders the image from the given viewpoint V_k with α -blending:

$$c(\mathbf{p}) = \sum_{n=1}^N \alpha_n c_n G_n^{2D}(\mathbf{p}) \prod_{i=1}^{n-1} (1 - \alpha_i G_i^{2D}(\mathbf{p})) \quad (3)$$

Here, c_n represents the view-dependent appearance of the current Gaussian primitive G_n^{2D} computed from SH coefficients, and $c(\mathbf{p})$ denotes the color at pixel \mathbf{p} . Rendering results will be used to calculate the loss against the ground truth and compute gradients. Through back propagation, the properties of Gaussian primitives can be adjusted instantly.

2DGS proposes flattening 3D Gaussian ellipsoids into 2D Gaussian elliptical disks. The planar-like shape of 2D Gaussian not only aligns more closely with the needs of surface reconstruction but also resolves the inconsistency in depth perception in 3DGS. As illustrated in Fig 3, this inconsistency arises when we observe Gaussian ellipsoids from different views, and the actual observed plane also varies. 2DGS constructs a local coordinate system for each 2D Gaussian. Any point $\mathbf{P}(u, v)$ in its local coordinate system can be transformed into its corresponding world coordinates with Gaussian center μ , two principal tangential vectors ($\mathbf{t}_u, \mathbf{t}_v$) and the scaling factors (s_u, s_v):

$$\mathbf{P}(u, v) = \mu + s_u \mathbf{t}_u u + s_v \mathbf{t}_v v = \mathbf{H}(u, v, 1, 1)^T \quad (4)$$

$$\text{where } \mathbf{H} = \begin{bmatrix} s_u \mathbf{t}_u & s_v \mathbf{t}_v & 0 & \mu \\ 0 & 0 & 0 & 1 \end{bmatrix} = \begin{bmatrix} \mathbf{RS} & \mu \\ \mathbf{0} & 1 \end{bmatrix} \quad (5)$$

$\mathbf{R} = [\mathbf{t}_u, \mathbf{t}_v, \mathbf{t}_w]$ is a 3×3 rotation matrix and $\mathbf{S} = [s_u, s_v, 0]$ is a 1×3 scaling matrix. $\mathbf{t}_w = \mathbf{t}_u \times \mathbf{t}_v$ is the normal vector of the local plane. In local coordinate system, value of the Gaussian primitive is expressed as standard 2D Gaussian.

To accurately calculate the ray-splat intersection, 2DGS proposes intersection strategy that can subsequently be used to compute depth. Additionally, 2DGS introduces depth distortion loss and normal loss to help the Gaussian primitives better conform to the scene surface. In light of the benefits outlined above, this paper adopts the Gaussian kernel and loss function proposed by 2DGS. For more detailed information, we recommend readers refer to the original paper.

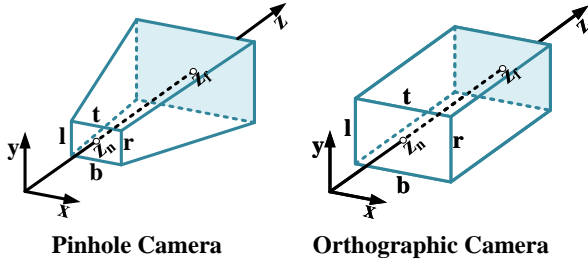


Fig. 4: Illustration of two camera models. In the projection transformation, we need to move the cone frustum or square frustum to the coordinate origin and scale it to the range of $[-1,1]$.

B. Orthographic Projection of 2DGS

3DGS employs a pinhole camera model to perform perspective projection on the centers of Gaussian primitives, with all rays projected from the optical center of the camera, and 2DGS follows the same approach. Perspective projection defines a prismoid as the visible space and compresses it into a small cube within the range $[-1,1]$. The perspective projection matrix is as follows:

$$\mathbf{M}_{presp} = \begin{bmatrix} \frac{2n}{l-r} & 0 & \frac{r+l}{l-r} & 0 \\ 0 & \frac{2n}{b-t} & \frac{t+b}{b-t} & 0 \\ 0 & 0 & \frac{z_f+z_n}{z_f-z_n} & \frac{2z_f z_n}{z_f-z_n} \\ 0 & 0 & 1 & 0 \end{bmatrix} \quad (6)$$

$$r = z_n \cdot \tan\left(\frac{\theta_x}{2}\right), t = z_n \cdot \tan\left(\frac{\theta_y}{2}\right) \quad (7)$$

z_n and z_f represent the distances from the near plane and far plane of the cone frustum to the camera's optical center, θ_x and θ_y denote the horizontal and vertical field-of-view angles of the camera, r, l, t, b correspond to the right, left, top, and bottom boundaries of the near plane of the cone frustum.

To obtain an orthographic image, we modify the projection method for the centers of the Gaussian primitives to orthographic projection. Shown as Fig 5, in the orthographic camera model, all rays are parallel to the optical axis of the

camera. These two camera models are both demonstrated in Fig 4. Orthographic projection defines a square frustum as the visible space, and the projection matrix is defined as follows:

$$\mathbf{M}_{ortho} = \begin{bmatrix} \frac{2}{r-l} & 0 & 0 & \frac{r+l}{r-l} \\ 0 & \frac{2}{t-b} & 0 & \frac{t+b}{b-t} \\ 0 & 0 & \frac{2z_n}{z_n-z_f} & \frac{z_n+z_f}{z_n-z_f} \\ 0 & 0 & 0 & 1 \end{bmatrix} \quad (8)$$

Under a given viewpoint, each point can achieve a 2D-to-2D orthographic mapping from local space to image space by left-multiplying the matrix $\mathbf{M}_{ortho} \mathbf{WH}$. Unlike the orthographic splatting in 3DGS that requires additional orthographic transformation of the covariance matrix, 2DGS eliminates that extra step.

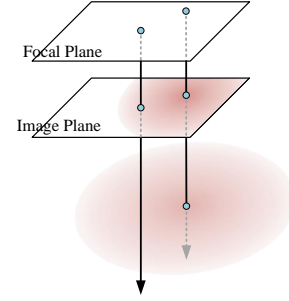


Fig. 5: Illustration of the degenerate solutions of 2DGS. We project the Gaussian position onto the image plane and create a standard 2D Gaussian centered at that point. By comparing the values at the intersection points of the current rays with the two Gaussians, we determine whether the 2D Gaussian has suffered from a degeneracy issue in the given view.

C. Orthographic Depth Maps

Generating an unbiased depth map corresponding to TDOM greatly facilitates the extraction of terrain and semantic information from the scene. For each pixel in the image, we calculate the termination depth of the corresponding ray using a method similar to volume rendering:

$$D = \sum_{i=0}^{N-1} \alpha_i T_i d_i \quad (9)$$

$$T_i = \prod_{j=0}^{i-1} (1 - \alpha_{j-1}) \quad (10)$$

where N denotes the count of Gaussians intersected by the ray, α_i represents the opacity at the ray-splat intersection \mathbf{x} , approximated by the Gaussian value $G_i(\mathbf{x})$ at the intersection. Meanwhile, d_i denotes the distance from the origin of the ray to the intersection \mathbf{x} . In the orthographic model, all rays are parallel to the camera's optical axis. The origin of each ray is designated as the intersection where the ray crosses a plane that passes through the camera optical center and is perpendicular to the ray. Clearly, the value of

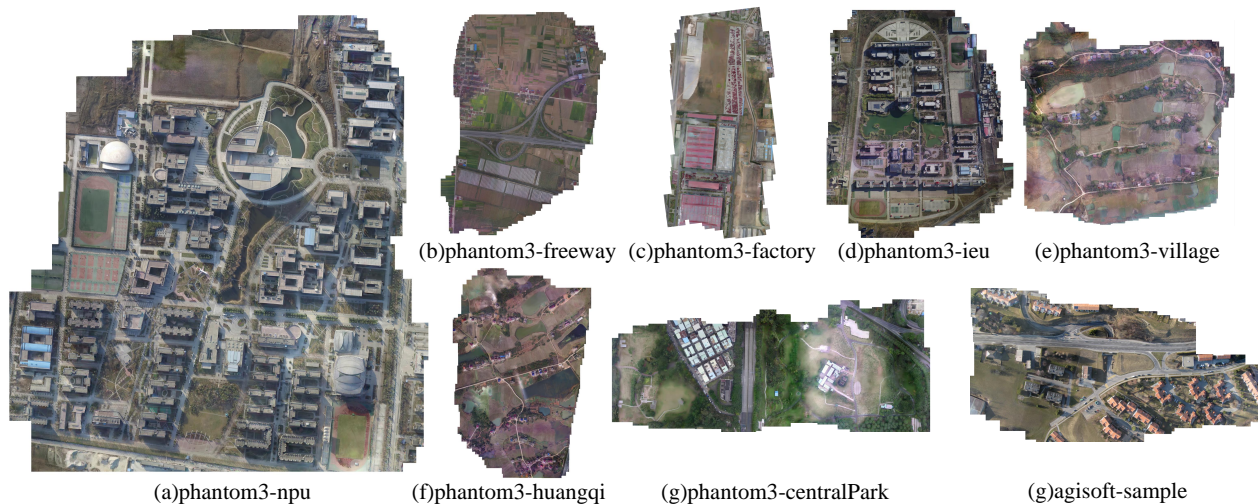


Fig. 6: An overview of the TDOM generated from the NPU DroneMap dataset and the Agisoft sample dataset by our proposed method.

d_i is equivalent to the z-axis coordinate of the Ray-splat intersection point in the view space.

Since 2D Gaussian primitives are elliptical disks, when observed from a specific viewpoint, the primitives can degenerate from surfaces into lines, which is a degeneracy issue present in 2DGS. Shown as Fig 5, When the Gaussian value $G_i(\mathbf{x})$ at the ray-splat intersection is too small, we create a standard 2D Gaussian distribution $g_i^{2D}(\mathbf{x})$, using the projection of the Gaussian primitive center on the image plane as the mean. By comparing the values at the intersections of the ray with the two Gaussians, when $g_i^{2D}(\mathbf{x})$ is greater than $G_i(\mathbf{x})$, the 2D Gaussian for the current view is considered degenerate, and d_i is taken as the z-axis coordinate of the Gaussian center in view space.

D. High-Resolution TDOM Rendering Strategy

The scale and complexity of large scenes lead to an explosion in the number of Gaussian primitives used to represent the scene, coupled with the parallel rendering of each pixel, subsequently resulting in a high demand for GPU memory when rendering high-resolution DOMs of large scenes. Inspired by Vast Gaussian, we apply a divide-and-conquer approach, progressively partitioning the scene data during training. The partitioning operation consists of three steps:

- **Camera position based scene partition:** We project the camera centers onto the ground and divide the scene into $m \times n$ cells, ensuring that each cell contains the same number of cameras.
- **Location based point selection:** We expand the boundaries of each cell by a preset ratio, project the point cloud onto the ground plane, and select the points within the boundaries as the data for the current partition.
- **Visibility based camera selection:** The visibility of the j-th cell to the i-th view is defined as Ω_{ij} / Ω_i , where Ω_i refers to the image area corresponding to the i-th view, Ω_{ij} refers to the projected area of the j-th cell's

bounding box in the i-th view. If the visibility exceeds a threshold, the i-th camera will be chosen for the current cell. Subsequently, the points covered by the i-th camera will be included in the cell.

The strategy of block-wise parallel training significantly reduces training time and mitigates the issue of insufficient GPU memory. For the same reason, we adopt batch rasterization to obtain the orthographic panorama with resolution comparable to the original images. The resolution of the generated image is adjustable which depends on the size of the view volume we set.

IV. EXPERIMENTS

In this section, we present evaluations of our TDOM generation method, including both qualitative and quantitative comparisons with some state-of-the-art commercial software. Furthermore, our depth maps have also been evaluated.

A. Experiments setup

Dataset: We selected several scenes with varying scales and characteristics from the NPU DroneMap Dataset[38], where the largest scene covers an area of 1.958 km². The chosen scenes include diverse land use types, including urban high-rise buildings, rural cottages, farmland, highways, and water bodies. The dataset was created by Bu et al., recorded using a custom-built hexacopter equipped with a GoPro Hero3+ camera and a DJI Phantom3. Each image has a 1920×1080 resolution. Moreover, we have also chosen a sample dataset provided by Agisoft [39], recorded by Canon DIGITAL IXUS 120 IS, which encompasses ground control point (GCP) information, to conduct a quantitative assessment of the TDOM's quality. The panoramic images generated by our method are shown in Fig 6.

Implementation: The initial point cloud and camera poses obtained from COLMAP sparse reconstruction first undergo Manhattan alignment to align the scene's bounding box with



Fig. 7: Comparison between those commercial software and our method, conducted on the NPU DroneMap dataset. Our approach better represents occlusion relationships and scene details. We mark the problematic areas in the images above with green borders.

the coordinate axes. Each scene is divided into 8 partitions following the progressive partition strategy. Training is conducted in two batches across 4 NVIDIA GeForce RTX 3090 GPUs for 60,000 iterations, during this period, the attributes of the 2D Gaussians are continuously optimized. After training, the gaussians are filtered according to their central positions using bounding boxes from camera-based scene partitioning. The average training time for a scene is around 7 hours. Soon, the processed points will be stitched and deduplicated for the subsequent rendering. We use the orthographic camera model mentioned in Section III-B to render orthophotos. The complete image is divided into 2×2 tiles and rendered one by one. When each pixel is rendered in the GPU unit, the orthographic depth is also calculated.

B. TDOM Evaluation

We selected four commercial software, namely Map2DFusion [38], ContextCapture [40], Metashape [41], and Pix4Dmapper [42], which are based on traditional TDOM generation methods, as comparisons to evaluate our method. All the methods use the same input images and configurations.

In the qualitative evaluation, we focused on buildings and thin structures.

- **Buildings:** In terms of high-quality TDOM, the buildings' edges must be continuous and sharp, and their facades must not be visible. Our method excellently reconstructs the building boundaries and their occlusion relationships. In Fig 7(a) and Fig 7(b), it can be observed that other methods generally exist visible building facades, with Map2DFusion showing the most severe issues due to direct photo mosaicking without image correction. Additionally, ContextCapture has blurred edges, Metashape displays noticeable irregular boundaries, and Pix4Dmapper suffers from misaligned building edges.
- **Thin structures:** Fig 7(c) and Fig 7(d) respectively demonstrate the restoration effects of the power tower and the air conditioner guardrail. Metashape consistently blurs and granulates scene information; the supports of the power tower become thickened and distorted in Map2DFusion, and are diminished in ContextCapture. The railings of the guardrail are significantly

TABLE I: Absolute distance error comparison between Metashape, ContextCapture, Pix4Dmapper and our method.

Pairs	GT(m)	Aligned Distance(m)				Absolute Error(m)↓			
		Metashape	ContextCapture	Pix4Dmapper	Ours	Metashape	ContextCapture	Pix4Dmapper	Ours
101-202	41.226	40.348	40.625	40.684	40.510	0.876	0.601	0.542	0.716
102-203	73.158	72.933	72.617	72.804	73.875	0.942	1.257	1.071	0.717
202-205	133.702	132.651	131.994	132.288	132.683	1.708	1.414	1.019	1.057
203-206	119.768	120.088	118.796	118.423	119.456	0.968	1.339	0.306	0.326
102-206	85.800	86.067	84.658	84.697	86.173	1.142	1.103	0.373	0.267
202-206	121.098	123.834	122.349	122.554	123.884	1.251	1.456	2.786	2.736

misaligned in all four software programs. In our method, these thin structures are clearer, and the details are well restored even under conditions of strong light and shadow contrast.

In the quantitative evaluation, the absolute distance error between two GCPs is applied as a criterion to evaluate the accuracy of the TDOM. We calculate the distances between the GCPs using both their true coordinate values and the coordinates extracted from the local coordinate system of the TDOM, while the true horizontal distances between the GCPs are computed using the Haversine formula. By aligning one pair of GCPs, we obtain a scaling factor, and then calculate the error between the aligned GCP distances from the TDOM and their true values. We compare our results with those from three commercial software solutions: Metashape, ContextCapture, and Pix4Dmapper. All the methods aligned the pair of control points GCP-101 and GCP-102. In our method, the minimum absolute error for GCP pairs is 0.267m, and the maximum absolute error is 2.736m. Our method maintains errors within 1.0m in the majority of cases and demonstrates comparable or superior accuracy relative to commercial software across most point pairs. Specific data can be found in Table I.



Fig. 8: Verification of the consistency between the depth map and TDOM. Column (1) replaces the R channel of the orthophoto with the depth map, and column (2) overlays the edges onto the orthophoto, which are extracted from the depth map using the Canny edge detection algorithm.

C. Depth Map Evaluation

We synthesize the depth map by calculating the termination depth of the ray corresponding to each pixel in the orthophoto using a method similar to volume rendering. In this section, we will qualitatively evaluate the consistency between our depth map and the TDOM.

In the qualitative experiments, we replace the Red channel of the orthophoto with the depth map to facilitate an intuitive visualization of the correspondence between the depth information and the image. Additionally, we use the Canny edge detection algorithm [43] to extract building edges from the depth map and overlay them onto our generated TDOM to observe the alignment of the edges. As illustrated in Fig 8(1), The deeper red hue in the pixel indicates the higher height of the relevant surface object relative to the ground. The red areas predominantly cover the buildings on the surface, which aligns with real-world logic. In Fig 8(2), the edges extracted from the depth map distinctly outline the boundaries of the structures within the TDOM, as well as some of the taller trees on the terrain. Our depth map adds a third dimension of height information to the TDOM, which is beneficial for subsequent tasks such as image detection and semantic segmentation in TDOM.

V. CONCLUSIONS

In this study, we propose a method based on differentiable rendering technology to generate large-scale, high-quality TDOM from UAV data without prior camera pose information. We progressively divide the scene into 8 blocks and use a 2DGS-based algorithm for parallel training on 4 GPUs. After fusing the point clouds, we perform batch rasterization to render orthophotos of the entire scene while simultaneously generating the corresponding depth maps. The results show that our method adapts well to different scenes, accurately represents building occlusion relationships, and reconstructs thin structures. Our TDOM with accuracy comparable to commercial software, combined with depth information, not only meets the demands of high-precision surveying and mapping but also provides users with more comprehensive and accurate spatial data support across multiple fields, thereby enhancing work efficiency and decision-making quality. However, our method still requires significantly longer training time per scene compared to commercial software. In future research, our aim is to improve the reconstruction efficiency of our method and further explore ways to save training resources.

REFERENCES

- [1] A. Habib, Y. Han, W. Xiong, F. He, Z. Zhang, and M. Crawford, "Automated ortho-rectification of uav-based hyperspectral data over an agricultural field using frame rgb imagery," *Remote Sensing*, vol. 8, no. 10, p. 796, 2016.
- [2] Y. Sheng, P. Gong, and G. S. Biging, "True orthoimage production for forested areas from large-scale aerial photographs," *Photogrammetric Engineering & Remote Sensing*, vol. 69, no. 3, pp. 259–266, 2003.
- [3] K.-S. Wu, Y.-r. He, Q.-j. Chen, and Y.-m. Zheng, "Analysis on the damage and recovery of typhoon disaster based on uav orthograph," *Microelectronics Reliability*, vol. 107, p. 113337, 2020.
- [4] B. A. DeWitt and P. R. Wolf, *Elements of Photogrammetry (with Applications in GIS)*. McGraw-Hill Higher Education, 2000.
- [5] T. Li, C. Jiang, Z. Bian, M. Wang, and X. Niu, "A review of true orthophoto rectification algorithms," in *IOP Conference Series: Materials Science and Engineering*, vol. 780, no. 2. IOP Publishing, 2020, p. 022035.
- [6] F. Amhar, J. Jansa, C. Ries, *et al.*, "The generation of true orthophotos using a 3d building model in conjunction with a conventional dtm," *International Archives of Photogrammetry and Remote Sensing*, vol. 32, pp. 16–22, 1998.
- [7] J. Rau, N. Chen, and L. Chen, "Hidden compensation and shadow enhancement for true orthophoto generation," in *Proceedings of Asian Conference on Remote Sensing 2000*, 2000, pp. 4–8.
- [8] K. Oda, W. Lu, O. Uchida, and T. Doihara, "Triangle-based visibility analysis and true orthoimage generation," *International Archives of Photogrammetry, Remote Sensing and Spatial Information Sciences*, vol. 35, no. Part 3, pp. 623–628, 2004.
- [9] A. F. Habib, E.-M. Kim, and C.-J. Kim, "New methodologies for true orthophoto generation," *Photogrammetric Engineering & Remote Sensing*, vol. 73, no. 1, pp. 25–36, 2007.
- [10] C. L. Zitnick and T. Kanade, "A cooperative algorithm for stereo matching and occlusion detection," *IEEE Transactions on pattern analysis and machine intelligence*, vol. 22, no. 7, pp. 675–684, 2000.
- [11] Y. H. Shin, S. W. Hyung, and D.-C. Lee, "True orthoimage generation from lidar intensity using deep learning," *Journal of the Korean Society of Surveying, Geodesy, Photogrammetry and Cartography*, vol. 38, no. 4, pp. 363–373, 2020.
- [12] Y. H. Shin and D.-C. Lee, "True orthoimage generation using airborne lidar data with generative adversarial network-based deep learning model," *Journal of Sensors*, vol. 2021, no. 1, p. 4304548, 2021.
- [13] J. T. Barron, B. Mildenhall, M. Tancik, P. Hedman, R. Martin-Brualla, and P. P. Srinivasan, "Mip-nerf: A multiscale representation for anti-aliasing neural radiance fields," in *Proceedings of the IEEE/CVF international conference on computer vision*, 2021, pp. 5855–5864.
- [14] J. T. Barron, B. Mildenhall, D. Verbin, P. P. Srinivasan, and P. Hedman, "Mip-nerf 360: Unbounded anti-aliased neural radiance fields," in *Proceedings of the IEEE/CVF conference on computer vision and pattern recognition*, 2022, pp. 5470–5479.
- [15] B. Kerbl, G. Kopanas, T. Leimkühler, and G. Drettakis, "3d gaussian splatting for real-time radiance field rendering," *ACM Transactions on Graphics*, vol. 42, no. 4, July 2023. [Online]. Available: <https://repo-sam.inria.fr/fungraph/3d-gaussian-splatting/>
- [16] S. Fridovich-Keil, A. Yu, M. Tancik, Q. Chen, B. Recht, and A. Kanazawa, "Plenoxels: Radiance fields without neural networks," in *Proceedings of the IEEE/CVF conference on computer vision and pattern recognition*, 2022, pp. 5501–5510.
- [17] S. Chen, Q. Yan, Y. Qu, W. Gao, J. Yang, and F. Deng, "Ortho-nerf: generating a true digital orthophoto map using the neural radiance field from unmanned aerial vehicle images," *Geo-spatial Information Science*, pp. 1–20, 2024.
- [18] X. Wang, W. Zhang, H. Xie, H. Ai, Q. Yuan, and Z. Zhan, "Tortho-gaussian: Splatting true digital orthophoto maps," 2024. [Online]. Available: <https://arxiv.org/abs/2411.19594>
- [19] B. Huang, Z. Yu, A. Chen, A. Geiger, and S. Gao, "2d gaussian splatting for geometrically accurate radiance fields," in *SIGGRAPH 2024 Conference Papers*. Association for Computing Machinery, 2024.
- [20] J. Lin, Z. Li, X. Tang, J. Liu, S. Liu, J. Liu, Y. Lu, X. Wu, S. Xu, Y. Yan, *et al.*, "Vastgaussian: Vast 3d gaussians for large scene reconstruction," in *Proceedings of the IEEE/CVF Conference on Computer Vision and Pattern Recognition*, 2024, pp. 5166–5175.
- [21] Y. Liu, C. Luo, L. Fan, N. Wang, J. Peng, and Z. Zhang, "Citygaussian: Real-time high-quality large-scale scene rendering with gaussians," in *European Conference on Computer Vision*. Springer, 2024, pp. 265–282.
- [22] X. WANG, W. JIANG, and J. XIE, "A new method for true orthophoto generation," *Geomatics and Information Science of Wuhan University*, vol. 34, no. 10, pp. 1250–1254, 2009.
- [23] K. I. Bang, A. Habib, C. Kim, and S.-W. Shin, "Comprehensive analysis of alternative methodologies for true ortho-photo generation from high resolution satellite and aerial imagery," in *American Society for Photogrammetry and Remote Sensing Annual Conference*, 05 2007.
- [24] C. Zhong, H. Li, Z. Li, and D. Li, "A vector-based backward projection method for robust detection of occlusions when generating true ortho photos," *GIScience & Remote Sensing*, vol. 47, no. 3, pp. 412–424, 2010.
- [25] Y. Sheng, "Minimising algorithm-induced artefacts in true ortho-image generation: a direct method implemented in the vector domain," *Photogrammetric Record*, vol. 22, no. 118, pp. 151–163, 2007.
- [26] G. Z. Wang Shu-gen, Li Deren and Z. Jinglin, "Method for information processing of shadows and occlusion on orthophotos," *Journal of Geomatics(Chinese)*, vol. 29, no. 4, pp. 1–4, 2004.
- [27] Q. Wang, L. Yan, Y. Sun, X. Cui, H. Mortimer, and Y. Li, "True orthophoto generation using line segment matches," *The Photogrammetric Record*, vol. 33, no. 161, pp. 113–130, 2018.
- [28] W. Yuan, X. Yuan, Y. Cai, and R. Shibasaki, "Fully automatic dom generation method based on optical flow field dense image matching," *Geo-spatial Information Science*, vol. 26, no. 2, pp. 242–256, 2023.
- [29] G. Zhou, *Urban High-Resolution Remote Sensing: Algorithms and Modeling*. CRC Press, 2020.
- [30] J. Yang, L. Liu, J. Xu, Y. Wang, and F. Deng, "Efficient global color correction for large-scale multiple-view images in three-dimensional reconstruction," *ISPRS Journal of Photogrammetry and Remote Sensing*, vol. 173, pp. 209–220, 2021.
- [31] M. Ebrahimikia and A. Hosseininaveh, "True orthophoto generation based on unmanned aerial vehicle images using reconstructed edge points," *The Photogrammetric Record*, vol. 37, no. 178, pp. 161–184, 2022.
- [32] M. Ebrahimikia, A. Hosseininaveh, and M. Modiri, "Orthophoto improvement using urban-snowflakenet," *Applied Geomatics*, vol. 16, no. 2, pp. 387–407, 2024.
- [33] B. Mildenhall, P. P. Srinivasan, M. Tancik, J. T. Barron, R. Ramamoorthi, and R. Ng, "Nerf: Representing scenes as neural radiance fields for view synthesis," *Communications of the ACM*, vol. 65, no. 1, pp. 99–106, 2021.
- [34] T. Müller, A. Evans, C. Schied, and A. Keller, "Instant neural graphics primitives with a multiresolution hash encoding," *ACM transactions on graphics (TOG)*, vol. 41, no. 4, pp. 1–15, 2022.
- [35] J. Lv, G. Jiang, W. Ding, and Z. Zhao, "Fast digital orthophoto generation: A comparative study of explicit and implicit methods," *Remote Sensing*, vol. 16, no. 5, p. 786, 2024.
- [36] B. Kerbl, G. Kopanas, T. Leimkühler, and G. Drettakis, "3d gaussian splatting for real-time radiance field rendering," *ACM Trans. Graph.*, vol. 42, no. 4, pp. 139–1, 2023.
- [37] J. L. Schonberger and J.-M. Frahm, "Structure-from-motion revisited," in *Proceedings of the IEEE conference on computer vision and pattern recognition*, 2016, pp. 4104–4113.
- [38] S. Bu, Y. Zhao, G. Wan, and Z. Liu, "Map2dfusion: Real-time incremental uav image mosaicing based on monocular slam," in *2016 IEEE/RSJ International Conference on Intelligent Robots and Systems (IROS)*. IEEE, 2016, pp. 4564–4571.
- [39] A. LLC, "Agisoft sample dataset," Online, 2022. [Online]. Available: <https://www.agisoft.com/zh-cn/downloads/sample-data/>
- [40] B. Systems, "Contextcapture viewer," Online, 2022. [Online]. Available: <https://www.bentley.com/software/contextcapture-viewer/>
- [41] A. LLC, "Metashape," Online, 2022. [Online]. Available: <https://photoscan.com/cn/>
- [42] Pix4D, "Pix4dmapper," Online, 2022. [Online]. Available: <https://www.pix4d.com/product/pix4dmapper-photogrammetry-software/>
- [43] J. Canny, "A computational approach to edge detection," *IEEE Transactions on pattern analysis and machine intelligence*, no. 6, pp. 679–698, 1986.